MNRAS 000, 1–12 (2023) Preprint 20 February 2024 Compiled using MNRAS LaTeX style file v3.0

A Model of Solar Magnetic Flux Rope Eruption Initiated Primarily by Magnetic Reconnection

Qingjun Liu,[1] Chaowei Jiang,[1,2]★ Xinkai Bian,[1] Xueshang Feng,[1,2] Pingbing Zuo,[1,2] and Yi Wang[1,2]
[1] *Shenzhen Key Laboratory of Numerical Prediction for Space Storm, Institute of Space Science and Applied Technology, Harbin Institute of Technology, Shenzhen 518055, China*
[2] *Key Laboratory of Solar Activity and Space Weather, National Space Science Center, Chinese Academy of Sciences, Beijing 100190, China*

Accepted XXX. Received YYY; in original form ZZZ

ABSTRACT

There is a heated debate regarding the specific roles played by ideal magnetohydrodynamic (MHD) instability and magnetic reconnection in the causes of solar eruptions. In the context with a pre-existing magnetic flux rope (MFR) before an eruption, it is widely believed that an ideal MHD instability, in particular, the torus instability, is responsible for triggering and driving the eruption, while reconnection, as invoked in the wake of the erupting MFR, plays a secondary role. Here we present a new numerical MHD model in which the eruption of a pre-existing MFR is primarily triggered and driven by reconnection. In this model, a stable MFR embedded in a strapping field is set as the initial condition. A surface converging flow is then applied at the lower boundary, pushing magnetic flux towards to the main polarity inversion line. It drives a quasi-static evolution of the system, during which a current layer is built up below the MFR with decreasing thickness. Once reconnection starts in the current sheet, the eruption commences, which indicates that the reconnection plays a determining role in triggers the eruption. By further analyzing the works done by in the magnetic flux of the pre-existing MFR and the newly reconnected flux during the acceleration stage of the eruption, we find that the latter plays a major role in driving the eruption. Such a model may explain observed eruptions in which the pre-eruption MFR has not reached the conditions for ideal instability.

Key words: Sun: Magnetic fields – Sun: Flares – Sun: corona – Sun: Coronal mass ejections – magnetohydrodynamics (MHD) – methods: numerical

1 INTRODUCTION

The magnetic fields in solar corona are line-tied at the solar surface (namely, the photosphere), and are often highly stressed as driven by continuous slow motions at the photosphere, for example, the large-scale shearing, rotational, and converging motions associated with magnetic flux emergence, and also the small-scale super-granular and granular convections. As such, magnetic energy is continually injected into the corona by the Poynting flux associated with the photospheric motions, and the free energy of the coronal magnetic field often builds up over several days during which the system evolves in a quasi-static way. At a critical point, there is a catastrophic disruption of this quasi-static evolution phase and magnetic energy releases rapidly, resulting in solar eruptions such as solar flares and coronal mass ejections (CMEs) with large clouds of magnetized plasma unleashed into the interplanetary space. Although solar eruptions have been observed for over a century, it remains unclear how solar eruptions are initiated, for which the key questions are how the eruption is triggered and what drives the acceleration of eruption. Current available theories can be classified into two categories, one is based on resistive magnetohydrodynamic (MHD) process (i.e., magnetic reconnection) and the other is based on ideal MHD process (i.e., ideal instabilities). There is a long-standing controversy on the specific roles of these two mechanisms in triggering and driving eruption, largely due to the difficulty in measuring directly the coronal magnetic fields (Yang et al. 2022).

The different mechanisms often assume different topologies of coronal magnetic field prior to eruption (Patsourakos et al. 2020). The reconnection-based mechanisms are developed based on sheared magnetic arcade, a single or multiple arcade configuration, for instance, the classic breakout model (Antiochos et al. 1999) and tether-cutting model (Moore et al. 2001). The magnetic breakout model requires the initial magnetic configuration of a quadrupolar topology that consists of an internal arcade and an external arcade with inverse directions to each other. As the internal arcade experiences shear motions along the polarity inversion line (PIL), it expands upward, leading to the formation of a current sheet and magnetic reconnection at the interface between the internal and external arcades. This reconnection continuously reduces the magnetic tension force that stabilizing the internal arcade,

---

★ E-mail: chaowei@hit.edu.cn (CWJ)

which can then expand outward (driven by its magnetic pressure force) and enhance the reconnection, therefore establishing a positive feedback loop. It results in the drastic eruption when the outward magnetic pressure force of the inner arcade dominates over the inward magnetic tension force. The tether-cutting model proposes that eruption can also be initiated with in a single sheared arcade. When the two J-shaped sheared magnetic loops gradually approach each other, an internal current sheet forms above the PIL, and then reconnection occurs in the current sheet. This reconnection plays a crucial role in reducing the downward tension of the magnetic arcades by effectively "cutting the tethers". Similar to the breakout model, this process, as going on, can eventually lead to eruption when the upward magnetic pressure force can no longer be restrained by the magnetic tension force. Recently, with a series of high-resolution MHD simulations, Jiang et al. (2021a) demonstrated that once an internal current sheet is formed in a strongly-sheared arcade, fast reconnection can immediately trigger an eruption, and the central engine for driving the eruption comes from the slingshot effect of the reconnection, i.e., the upward magnetic tension force of the newly reconnected field lines. Therefore, reconnection plays a fundamental role in both triggering and driving the eruption from a sheared arcade magnetic configuration.

The ideal MHD instability mechanisms are developed based on magnetic flux rope (MFR), which is a coherent group of magnetic field lines winding about a common axis by over one full turn (Cheng et al. 2017; Liu 2020). In this framework, two primary models for initiation of eruption have been proposed, including the kink instability (Hood & Priest 1979; Török & Kliem 2005, 2007; Guo et al. 2022) and the torus instability (Kliem & Török 2006; Aulanier et al. 2010; Fan & Gibson 2007). The kink instability arises when the degree of helical twisting of field lines around the rope's axis exceeds a critical threshold. This threshold is typically in the range of 1.25 $\sim$ 2.5 turns of winding of the field lines (Mikic et al. 1990; Fan & Gibson 2003; Török & Kliem 2003; Török & Kliem 2005; Török et al. 2004). As a result of this instability, an eruption is triggered with rapid writhe of the MFR axis (thus its center part rises impulsively), while the field lines around the axis unwinds. This process is accompanied by the release of the stored magnetic energy within the flux rope. However, the kink instability saturates quickly and cannot drive a full eruption, which needs the onset of the other instability, i.e., the torus instability. It describes the loss of force balance between the MFR and the overlying field (or the external field).[1] The upward forces, consisting of magnetic pressure and hoop force of the MFR, counteract the downward confinement forces of magnetic tension of the overlying field. This instability arises when the external strapping field decay sufficiently rapidly with height, causing the upward forces on the MFR to surpass the downward forces during its rise. As a result, the MFR undergoes a continuous uplift, as driven by the net upward force. To quantify the rate of decay of the external strapping field, a decay index is introduced as $n(z) = -\partial \ln B_e / \partial \ln z$ (Bateman 1978), where B_e is the external field and z the height or radial distance from solar surface. Theoretical analyses predict that the critical threshold for the occurrence of torus instability is approximately $n_c = 1.5$ (but still with a wide range of 1.1 $\sim$ 1.7 depending on the specific geomoetry of the MFR, e.g., Kliem & Török 2006; Török & Kliem 2007; Fan & Gibson 2007; Aulanier et al. 2010; Démoulin & Aulanier 2010; Fan 2010; Zuccarello et al. 2015), and when the MFR axis reaches the domain with $n(z) > n_c$, it can erupt successfully.

Although a pre-existing MFR can be activated by the aforementioned ideal instabilities, reconnection is unavoidably associated with its subsequent eruption. This is due to the stretching of the overlying magnetic field by the erupting MFR, leading to the dynamic formation of a current sheet beneath it. Then reconnection is triggered at the current sheet, producing a flare with the eruption of the MFR. It is generally believed that in this process, the eruption is driven mainly by the ideal instability (in particular, the torus instability), while the flare reconnection is only a by-product of the eruption and plays a secondary role in driving the eruption by transferring the overlying flux into the MFR. In this paper we present a three-dimensional (3D) numerical MHD model that is at variance with this conventional view. We demonstrate a case in which the eruption of a pre-existing MFR is primarily triggered and driven by reconnection. The simulation is started from a stable MFR embedded in a strapping field, and then a converging flow is applied at the bottom surface (i.e., the photosphere) to the strapping field. The converging motion drives a quasi-static evolution of the system, during which the decay index at apex of the MFR axis slowly increases and meanwhile a current layer is built up below the MFR with decreasing thickness. At a critical point when the decay index is very close to the canonical threshold of $n_c = 1.5$, the MFR erupts, suggesting that the torus instability sets in. Interestingly, the start of the eruption also coincides with the onset of reconnection in the current sheet as formed from thinning of the current layer during the quasi-static evolution phase. This is confirmed by experiments of different grid resolutions, from which it is found that with higher resolution the eruption onset time is delayed, since a thinner current sheet can be supported and thus the reconnection is also delayed. This indicates that the reconnection plays a determining role in triggers the eruption. By further analyzing the works done by in the magnetic flux of the pre-existing MFR and the newly reconnected flux during the acceleration stage of the eruption, we find that the latter plays a major role in driving the eruption.

2 NUMERICAL MODEL

We used the conservation element and solution element (CESE) method implemented on an adaptive mesh refinement (AMR) grid with parallel computing, namely, the AMR–CESE–MHD code (Jiang et al. 2010) to solve the full MHD equations in a 3D Cartesian geometry. The MHD equa-

---

[1] The overlying field is also referred to as the background field, the external field, or the strapping field, which are all used interchangeably in the context of describing torus instability.

tions are given as

$$\frac{\partial \rho}{\partial t} + \nabla \cdot (\rho \mathbf{v}) = 0,$$
$$\rho \frac{D\mathbf{v}}{Dt} = -\nabla p + \mathbf{J} \times \mathbf{B} + \nabla \cdot (\nu \rho \nabla \mathbf{v}),$$
$$\frac{\partial \mathbf{B}}{\partial t} = \nabla \times (\mathbf{v} \times \mathbf{B} - \eta \mu_0 \mathbf{J}),$$
$$\frac{\partial T}{\partial t} + \nabla \cdot (T\mathbf{v}) = (2-\gamma) T \nabla \cdot \mathbf{v}, \tag{1}$$

where $\mathbf{J} = \nabla \times \mathbf{B}/\mu_0$ and μ_0 is the magnetic permeability in a vacuum. The momentum equation includes a term for kinetic viscosity with a small coefficient ν given by $\nu = 0.05\Delta x^2/\Delta t$, where Δx is the local spatial resolution and Δt is the time step. Since the fully ionized plasma in the real corona is highly conductive, we chose to not use explicit resistivity in the magnetic induction equation, but magnetic reconnection can still be triggered through numerical diffusion when a current layer is sufficiently narrow with thickness close to the grid resolution. By this, we achieved an effective resistivity as small as we can with given grid resolution. In the energy equation, the adiabatic index is set to $\gamma = 1$, which thus reduces to an isothermal process.

To investigate the role of reconnection and torus instability in initiating the eruption of a pre-existing MFR, we first construct an initial magnetic configuration that contains a stable MFR. In numerical simulations, there are various approaches to building an MFR. These include the transformation from magnetic arcades to MFR through slow reconnection driven by flux cancellation flows (Amari et al. 2003b; Linker et al. 2003; Aulanier et al. 2010; Zhang et al. 2022), the process of magnetic flux emergence and its associated dynamic (Fan 2001; Leake et al. 2013; Liu et al. 2023), the formation of MFR through magnetic helicity condensation driven by supergranular and granular motions (Liu & Xia 2022), and the utilization of semi-analytical models for coronal MFRs (Titov & Démoulin 1999; Titov et al. 2014, 2018). Here we opted to employ the semi-analytical, near force-free Titov-Demoulin-modified (TDm) model (Titov et al. 2014, 2018) to construct the initial magnetic configuration. This choice was made because the alternative methods as aforementioned are more complex and often require more time to form an MFR. By utilizing the TDm model, we can efficiently establish the desired magnetic configuration and proceed to investigate the role of reconnection and ideal instability in initiating the eruption.

The initial condition of our simulation is established by combining two methods: the regularized Biot-Savart laws (RBSL) method (Titov et al. 2018), which constructs the TDm model (Guo et al. 2019), and the MHD relaxation method (Jiang et al. 2021b), which allows us to obtain an MHD equilibrium state from the near force-free field of TDm model. The TDm model incorporates four independent parameters that govern the structure of the MFR and the background magnetic field. These parameters include the path of the axis ς, the minor radius, the magnetic flux F, and the electric current of the flux rope. The path of the axis follows an iso-contour, B_q = const (the background field), which takes the form of a circular arc in the vertical plane of symmetry of the configuration. This circular arc is closed by a sub-photospheric arc ς^*, forming a circle with a radius of $R = 75$ Mm. The radius of the torus is set to $a = 20$ Mm. The typical magnetic flux is determined by averaging the absolute values of the magnetic flux within the radius of the torus from the two footprints of the flux rope, namely, $F = (|F_+| + |F_-|)$. The typical electric current is calculated as $I = 5\sqrt{2}/(3\mu_0 a)$. The background field B_q is modeled by two points sources below the bottom boundary.

Since the TDm magnetic field is not accurately force-free, it is further relaxed to an MHD equilibrium with a background plasma atmosphere. The plasma is initially an isothermal gas of temperature $T = 1 \times 10^6$ K in hydrostatic equilibrium and stratified by the solar gravity with density $\rho = 2.29 \times 10^{-15}$ g cm^{-3} at the bottom. The values for temperature and density are typical in the corona. At the bottom boundary, the magnetic field evolves according to magnetic induction equation by treating the bottom boundary as a perfectly line-tying and fixed surface (with zero velocity) for magnetic field lines. It is important to note that this does not imply that all magnetic field components are fixed on the boundary because although the velocity is zero at the bottom boundary, it may not be zero at neighboring inner points. Therefore, the horizontal components of magnetic field can vary with time, until all velocity approaches zero. Figure 1A shows the relaxed magnetic field configuration of the TDm model, with colors representing the value of non-linear force-free factor $\alpha = \mathbf{J} \cdot \mathbf{B}/B^2$. This mimics a typical coronal magnetic configuration with a low-lying MFR along the PIL stabilized by the overlying near-potential field, and the decay index at the apex of the rope axis is 0.6.

With the MHD equilibrium containing a stable MFR configuration as the initial condition, we drove its evolution by introducing a surface converging flow (Amari et al. 2003a) at the bottom boundary defined as

$$v_x = -c_0(B_q)_z, v_y = 0, v_z = 0 \tag{2}$$

where c_0 is a constant for scaling such that the largest velocity is 7.4 km s^{-1} and $(B_q)_z$ refers to the vertical component of the background field at the bottom boundary at the initial time. Such a converging flow can effectively inject magnetic energy into the system and increase the decay index at the apex of MFR axis by modifying the flux distribution of the background field, therefore driving the system to approach an unstable state. Also, the converging motion is favorable for formation of an internal current sheet above the PIL and subsequent triggering of reconnection (Bian et al. 2022a). Figure 1B shows the distribution of the magnetic field on the bottom surface, where the arrows represent the converging velocity.

The simulation volume used in our study is a cube with dimensions of $[-230, 230]$ Mm in both x and y direction, and $[0, 460]$ Mm in z direction. This size was chosen to be much larger than the initial MFR structure, thus allowing sufficient space for simulating the eruption initiation process of the MFR without the influence from the side and top boundaries.[2] The plasma density, temperature, and velocity were fixed on the side and top boundaries. Furthermore, the horizontal components of the magnetic field were linearly extrapolated from the inner points, while the normal component was modified to satisfy the divergence-free condition, thus

---

[2] All the simulation runs in this work are stopped before the disturbance by the eruption reaches any of the side and top boundaries.

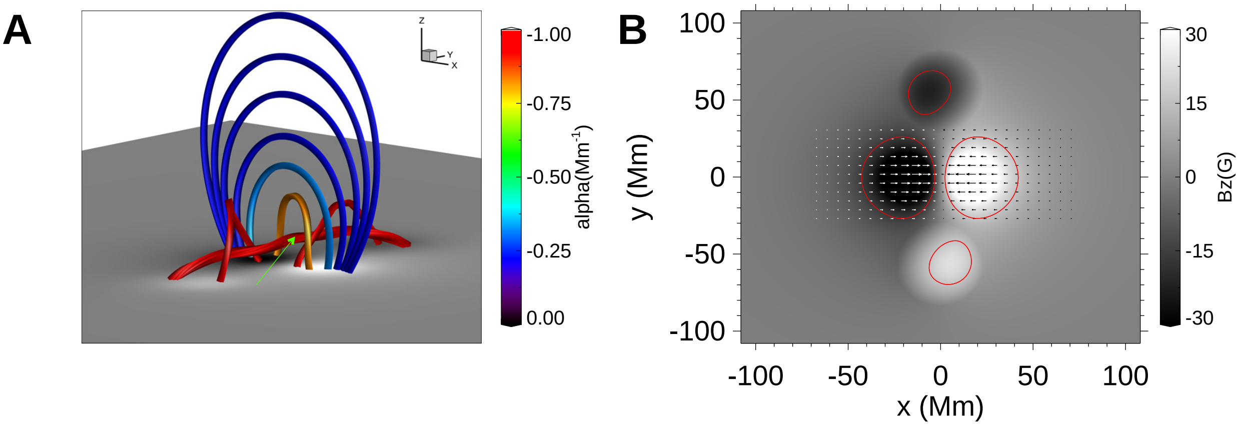

Figure 1. Initial magnetic field (A) and bottom driving flow (B) of the MHD simulation. In panel A, the field lines are shown by the thick lines, which are colored by the value of the nonlinear force-free factor defined as $\alpha = \mathbf{J} \cdot \mathbf{B}/B^2$. The green arrow points out the axis of magnetic flux rope. The bottom surface is shown with the magnetic flux distribution. In panel B, the driving flow at the bottom surface is shown by the arrows, and the background also shows the magnetic flux distribution . The red contour lines indicate the main magnetic polarities.

preventing any numerical magnetic divergence from accumulating at the boundaries.

The entire simulation volume is resolved using a block-structured AMR grid. We have carried out three set of simulations (to be referred to as RES0, RES1, and RES2), in which the base resolution is identical with $\Delta x = \Delta y = \Delta z = \Delta = 2.88$ Mm and the highest resolution is, respectively, $\Delta = 180$ km, 90 km, and 45 km. The highest resolution in the simulations is used to resolve the core region of the computational volume with strong magnetic field and current density (for instance, the region encompassing the MFR), and also to dynamically capture thin layers of enhanced current density that may develop into current sheet. By using the different-resolution experiments, we can test whether our calculation converges in the ideal MHD regime. A more important consideration for performing the experiments on different resolutions is that, with all other settings being the same, in the simulation of a higher resolution a current sheet can be thinner and thus the onset of reconnection will be later than that of a lower resolution. This is because, as we have mentioned before, the reconnection results from numerical diffusion when the thickness of the current sheet is close to the grid resolution. In this sense, the onset time of reconnection depends on the grid spacing, because, with a smaller grid size, a thinner current sheet can develop and sustain a stronger current density (and therefore more free energy), which needs more time to accumulate. Therefore, the onset of reconnection in the current sheet is postponed relative to runs with lower resolutions. The dependence of reconnection onset time and the effective resistivity on the grid resolution in our MHD code has been carefully studied in previous simulations (Jiang et al. 2021a).

3 RESULTS

As driven by the converging motion, the coronal magnetic field first undergoes a quasi-static evolution and then runs into a drastic eruption, as depicted by the 3D magnetic field lines in Figure 2 (and the animation) and the energy curves in Figure 3. In the quasi-static evolution stage, the overlying field expands slowly which allows a continuous rise of the MFR but the system maintains in proximity to a force-free state. The magnetic energy increases almost linearly, while the kinetic energy remains negligible as compared with the magnetic energy. This suggests that almost all the energy as injected into the corona by the surface flow through the Poynting flux is stored in the magnetic field. At a critical point, i.e., onset of the eruption, the MFR starts to rise rapidly along with reconnection in its wake. During the eruption, the kinetic energy increases impulsively by nearly two orders of magnitude in a very short period of around 5 min, indicating the rapid acceleration of the plasma. Despite the continual injection of Poynting flux through the bottom surface, the magnetic energy drops immediately, indicating a quick release of magnetic energy during the eruption. From the energy curves, it can be seen that the eruption starts at different moments in the three simulation runs with incremental higher resolution from RES0 to RES2, which are $t = 50$ min 09 s, 53 min 02 s, and 56 min 07 s, respectively. We have also carried out a test run of RES0 by stopping the surface driving motion once the eruption begins (see the dashed curves in Figure 3), and validated that the eruption, once triggered, is almost not affected by the slow surface driving motion.

Figure 4A depicts the time evolution of the apex height of the MFR axis and also the corresponding decay index of the strapping field there. The simulations all show that the height curves of the MFR axis exhibit a gradual growth before the eruption, and then rises rapidly with onset of the eruption. The slow rise of the MFR with a speed of around 10 km s^{-1}

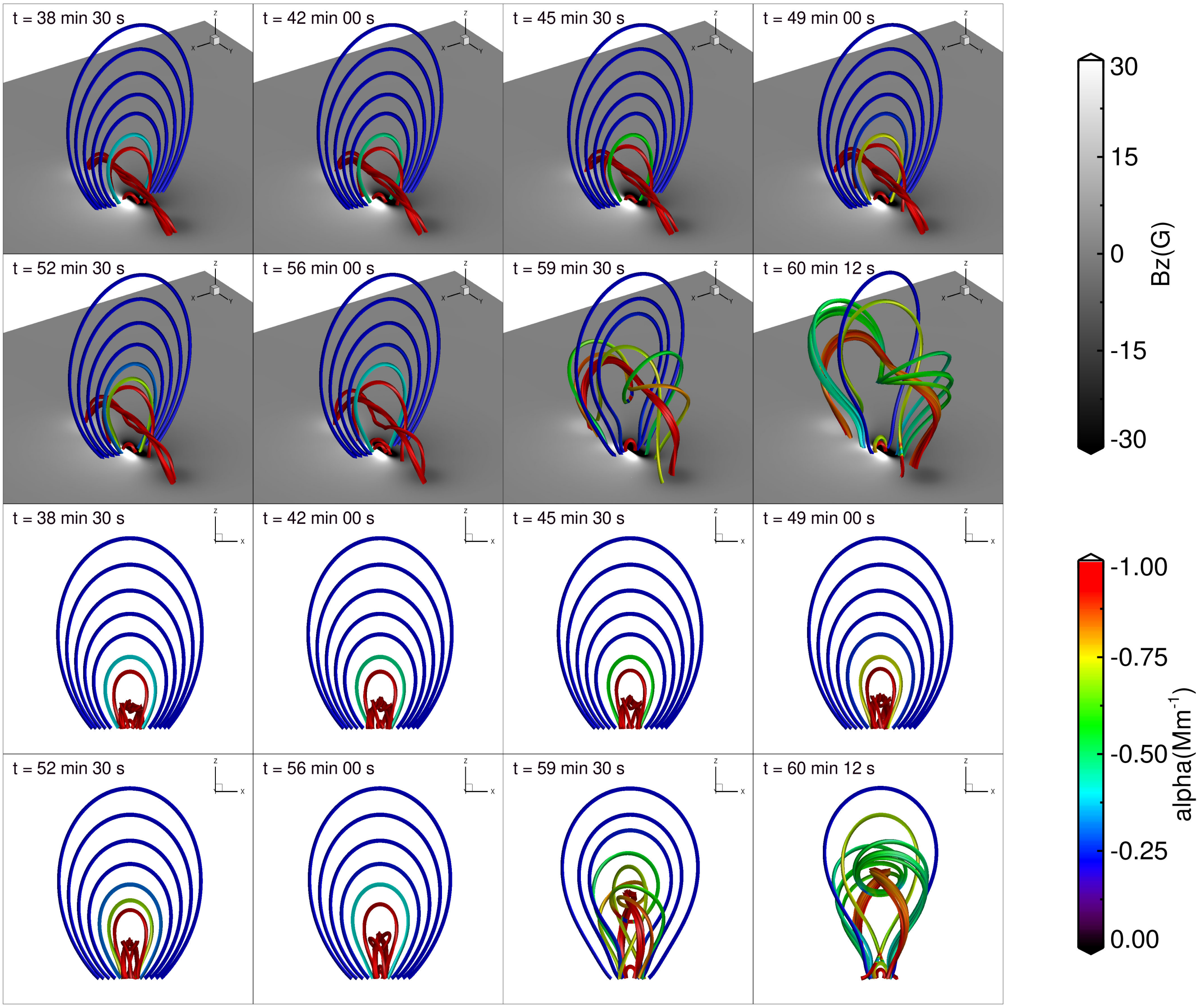

Figure 2. Evolution of magnetic field lines in the simulation. (A) The 3D prospective view of magnetic field lines. The colored thick lines represent magnetic field line and the colors denote the value of $\alpha = \mathbf{J} \cdot \mathbf{B}/B^2$, which indicates how much the field lines are non-potential. (B) side view of the same field lines shown in (A). An animation is provided.

in 20 minutes before the eruption onset is consistent with many observations that shows filaments often rise slowly before they erupt more quickly (Zhang et al. 2001; Sterling & Moore 2005; McCauley et al. 2015). Prior to the eruption the decay index grows almost linearly, even in the early phase (for example, from $t = 0$ to 30 min) when the amount of rise of the MFR axis is very small. This is because the decay index is changed in a larger portion due to variation of the strapping field (as driven by the converging flow) than the rise of the MFR. Importantly, the decay index increases continuously from the initial value of 0.6 to a value very close to the canonical threshold $n_c = 1.5$ at which the eruption immediately begins. This good consistence of the eruption onset with the threshold condition of the torus instability appears to indicate that the eruption of the MFR is triggered by torus instability. Nevertheless, whether the torus instability can actually occur also depends on the details of the MFR itself rather than solely the decay index of the external field. Correspondingly, the critical decay index for torus instability has a wide range of around $1.1 \sim 1.7$ rather than the specific number of 1.5, which has been mentioned in Section 1. More intricately, in some case, for example as shown in a failed eruption model recently developed by Jiang et al. (2023), an MFR erupts with the decay index at its axis being as small as 1, while the eruption is halted even when the decay index at the MFR axis has reached around 2.5! Therefore it is still unclear whether the torus instability sets in by only calculating the decay index. To look into whether there is really a loss of force balance at the axis of the MFR at the eruption onset time, which is predicted by the torus instability, we calculated the upward and downward forces at the axis. They are defined respectively as $F_z^{\mathrm{upward}} = (\mathbf{J} \times \mathbf{B}_{\mathrm{MFR}})_z$,

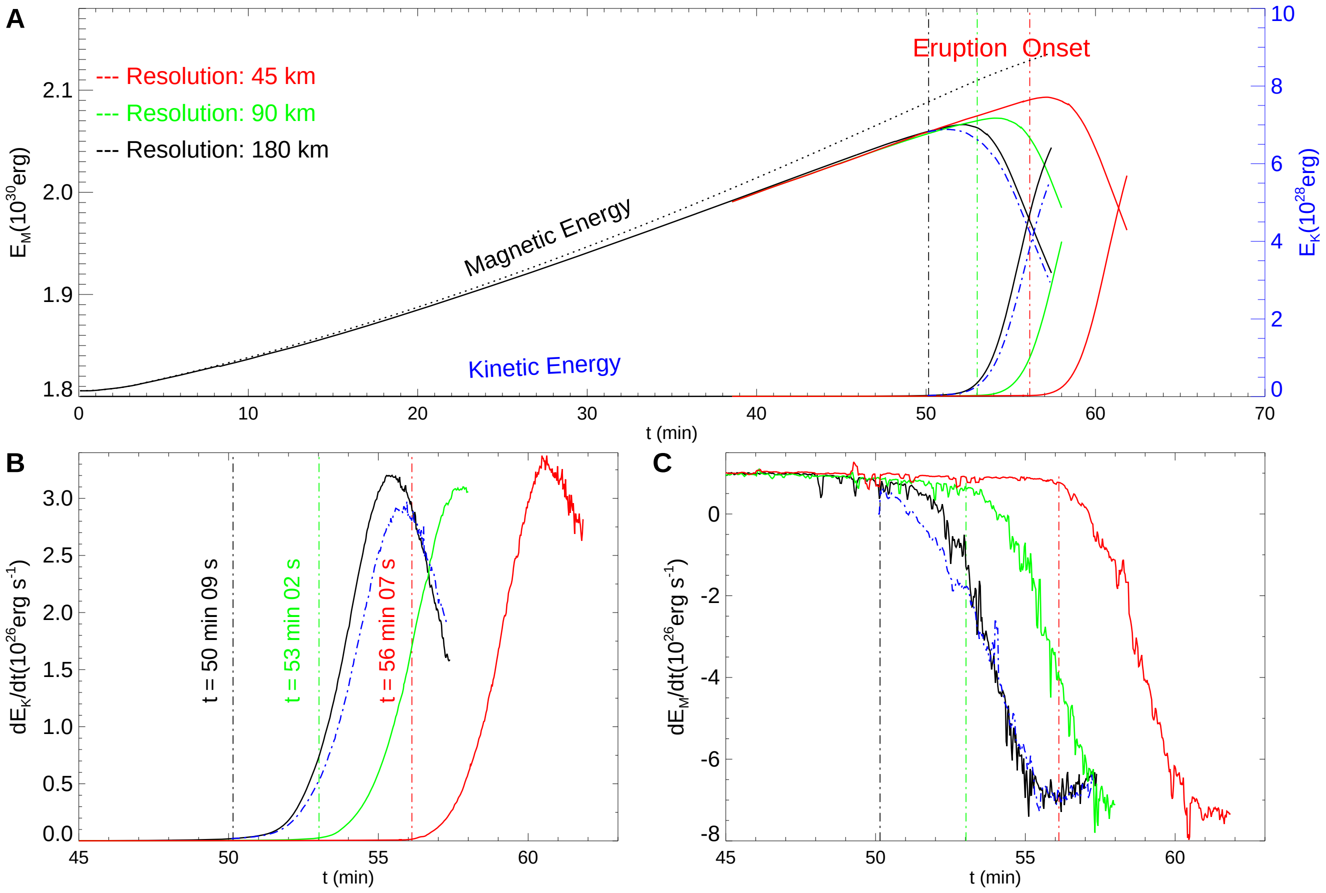

Figure 3. Evolution of different parameters of energies in the simulation runs with different grid resolutions. (A) Magnetic energy E_M and kinetic energy E_K. The colors of the curves denote the results of the different runs; black for RES0, green for RES1, and red for RES2. The dotted curve shows the energy injected into the volume (i.e., time integration of total Poynting flux) from the bottom boundary through the surface flow. The blue dot-dashed curves show the result for RES0 with the bottom driving flow stopped once the eruption is triggered. (B) Increasing rate of kinetic energy dE_K/dt. (C) Releasing rate of magnetic energy dE_M/dt. In all panels, the vertical dot-dashed lines mark the eruption onset times, which are different in the different runs, as denoted by the numbers in panel B.

and $F_z^{\text{downward}} = (\mathbf{J} \times \mathbf{B}_e)_z$ (where $\mathbf{B}_{\text{MFR}}$ is the magnetic field of the MFR and $\mathbf{B}_e$ the strapping field). The evolution of these two forces is shown in Figure 4B. Both the two forces decrease with time and thus with height since the axis rises continuously. However, these forces are well balanced, even at the eruption onset time, suggesting that the torus instability is not actually triggered.

On the other hand, the simulations indicate the importance of reconnection in triggering the eruption. As shown in Figure 5, a thin current layer is formed below the MFR during the quasi-static evolution stage, as driven by the slow converging motion at the bottom surface. The current layer gradually becomes thinner, especially in its core region where the current density is the highest. Figure 5C shows the time variation of the thickness of the current layer. The thinning of the current layer occurs quasi-statically. Eventually, the current layer evolves into a current sheet as it thins down to a spacing of around 3 grids, leading to reconnection in the current sheet. The magnetic field component B_z crossing the current sheet shows a thinning down to a tangential discontinuity in numerical sense. The moment at which the current sheet forms and reconnection sets in is exactly the same as the eruption onset time in the different resolution runs. As can be seen in Figure 5D, the start of reconnection in the different runs is also indicated by the sudden rise of the maximal velocity $v_{\max}$ in the computational volume. This is because the sharp variation of the maximal velocity occurs in the reconnection outflow region, where the plasma is impulsively accelerated upward (see also the right column of Figure 6).

Both the height profile of the MFR axis (Figure 4) and the energy evolutions (Figure 3) show that the eruption onset is sensitive to the resolution, as it is postponed by about 3 min incrementally from RES0 to RES3. This is because, as has been noted near the end of Section 2, at a higher resolution a current sheet can be thinner and the onset time of reconnection is postponed (see Figure 5C). Our analysis indicates that the reconnection of the core current sheet plays a more important role in determining the onset of the eruption (and fast rise of the MFR) than the torus instability. Otherwise, an eruption as initiated totally by an ideal MHD process will

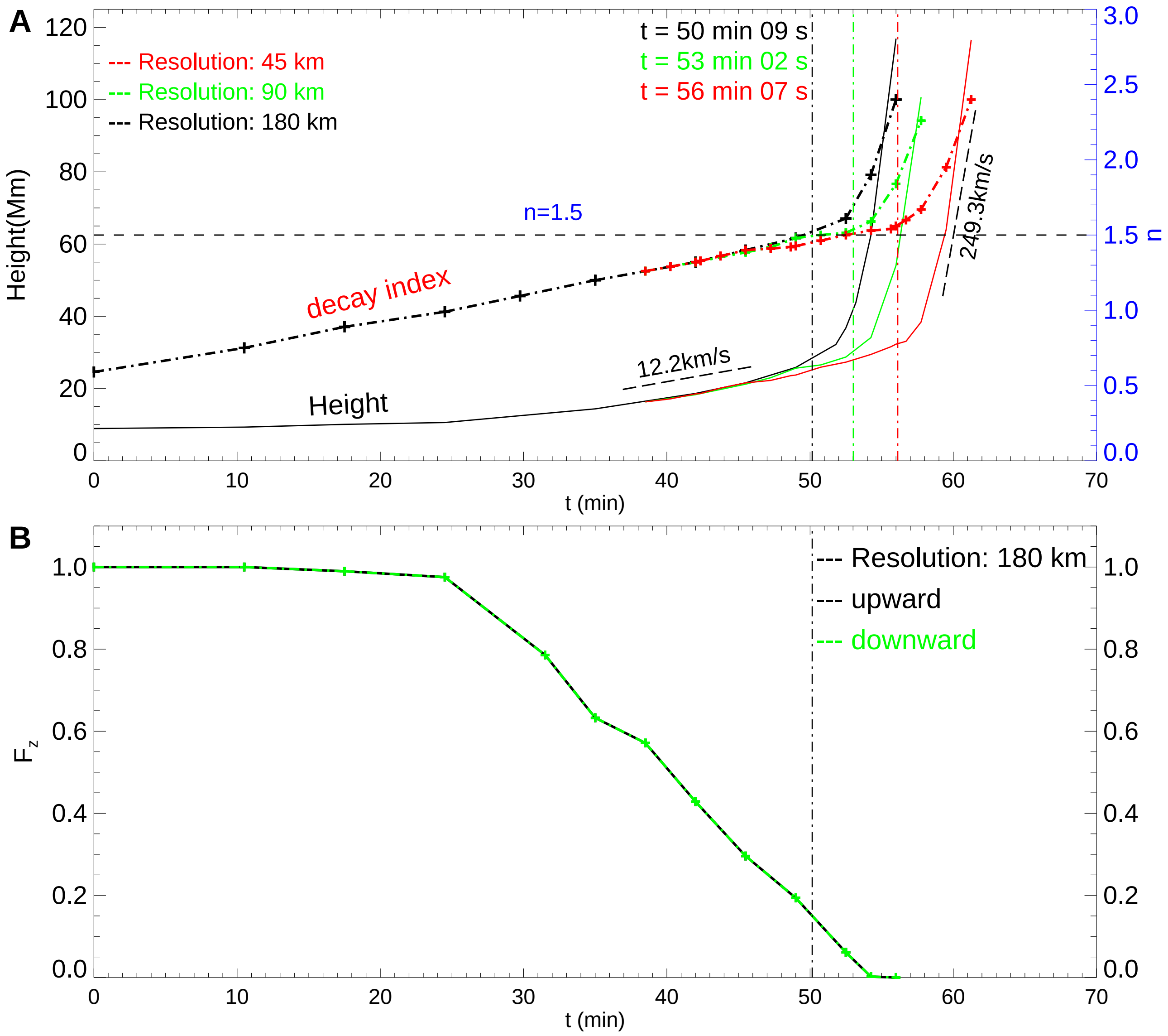

Figure 4. Evolution of different parameters of the MFR in the simulation. (A) Apex height (solid lines) of the MFR axis and the decay index (dashed lines) of the strapping field at the apex of the MFR axis. Colors of the lines are used to denote the results in the different runs from RES0 to RES2. The horizontal dashed line denotes the critical height for decay index $n = 1.5$. The vertical dashed dotted lines denote the onset times of the eruptions. The average speed of the MFR axis in the slow rise phase and during the eruption is shown with the oblique dashed lines. (B) The upward (colored in black) and downward (green) components of Lorentz force at the apex of the MFR axis. They are defined respectively as $F_z^{\mathrm{upward}} = (\mathbf{J} \times \mathbf{B}_{\mathrm{MFR}})_z$, and $F_z^{\mathrm{downward}} = (\mathbf{J} \times \mathbf{B}_e)_z$ (where $\mathbf{B}_{\mathrm{MFR}}$ is the magnetic field of the MFR and $\mathbf{B}_e$ the strapping field). Result is shown for RES0 run. Note that the two plots overlay each other almost exactly, indicating that the upward and downward forces are nearly exactly balanced over the entire period.

not be affected by the grid resolution since the here the lowest RES0 is already high enough to resolve the ideal MHD process.

To further investigate the source of driving force for the acceleration of the eruption, we divide the flux (and thus the volume) of entire erupting MFR into two components and calculate the works done by these two components separately, for the aim of distinguishing the roles of the ideal instability and the reconnection played in driving the eruption. Specifically, one component, referred to as the “original component”, is the magnetic flux originated from the pre-existing MFR before the eruption. This component expands in volume but remains to be the same magnetic flux during the eruption, and if the MFR evolves ideally without reconnection, the eruption will be driven by only this component. Therefore, the work by Lorentz force in the original component corresponds to contribution of the ideal instability. The other component is the flux newly incorporated into the

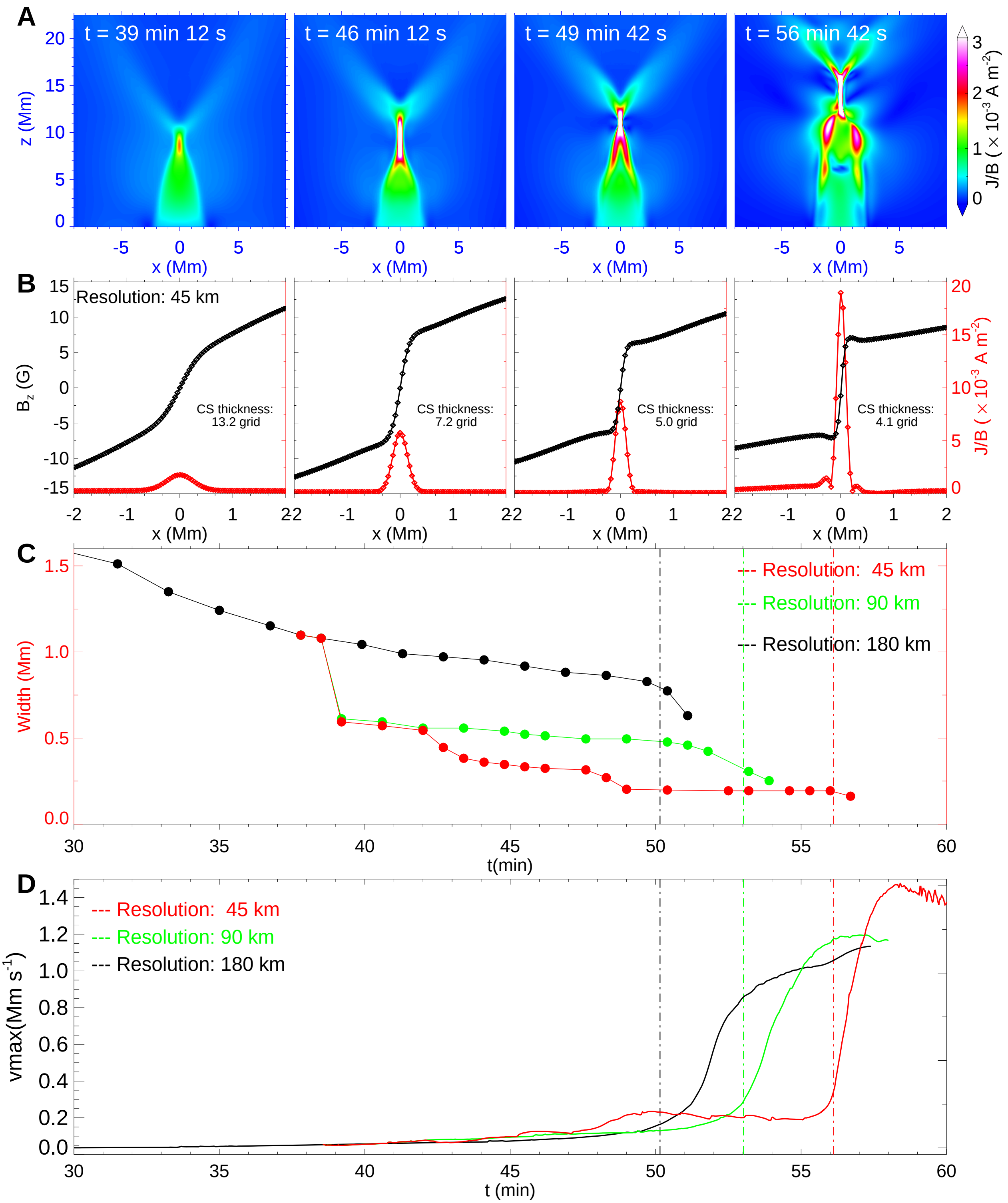

Figure 5. Formation of current sheet and onset of reconnection. (A) Distribution of current density J normalized by magnetic field strength B on the vertical cross section (the $y = 0$ slice). (B) 1D profile of the magnetic field component B_z and J/B along a horizontal line crossing perpendicular to center of the current sheet (which is defined as the point with largest J/B). The diamonds denote values on the grid nodes. (C) Thickness evolution of the current sheet before the eruption onset. The results are shown for all the three runs from RES0 to RES2. (D) The largest velocity in the three different runs. . The vertical dashed lines show the onset time of eruptions in the different runs.

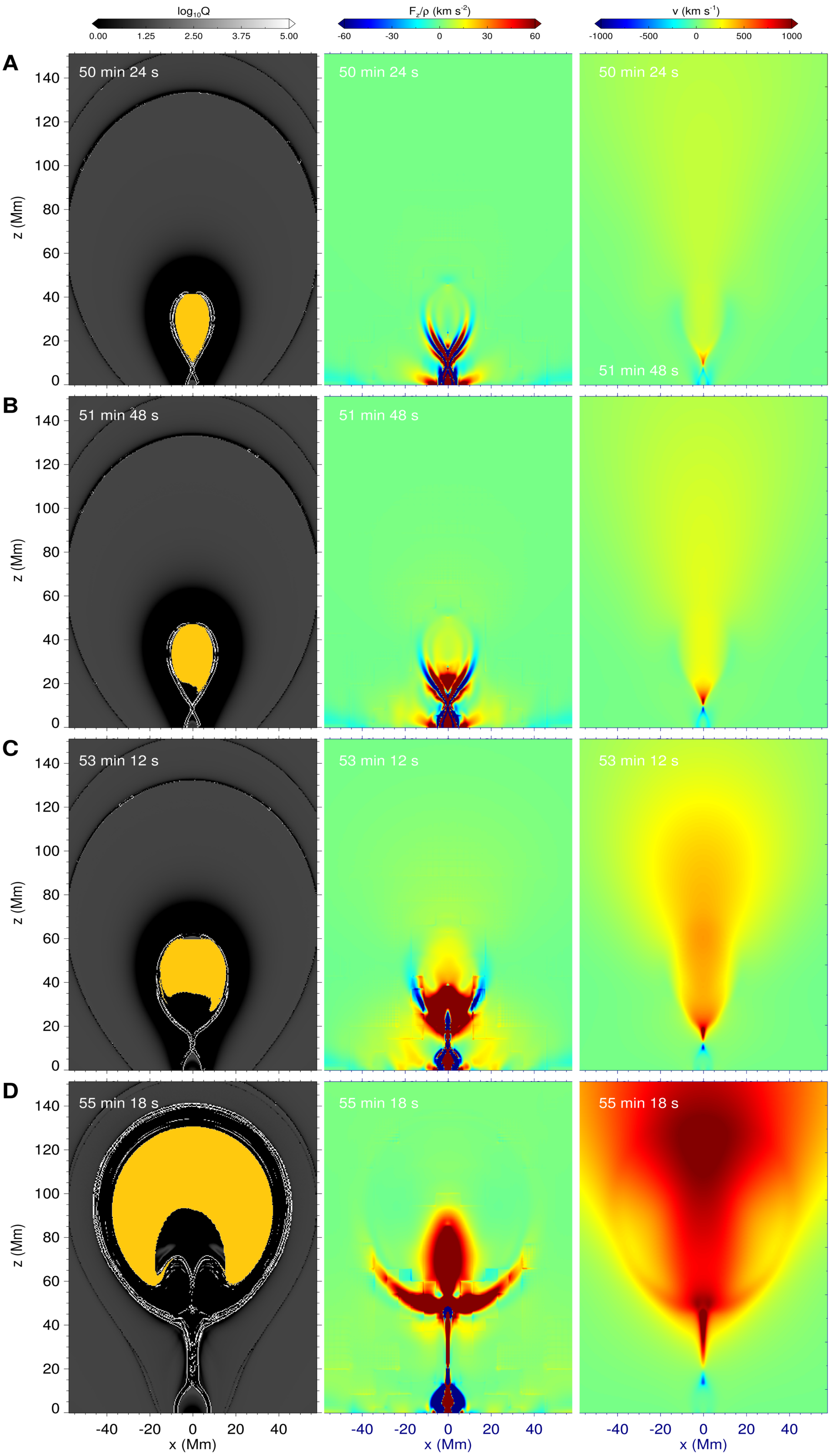

Figure 6. Eruption of the MFR as shown at the central vertical cross section $y = 0$ slice. Left: The magnetic squashing factor Q. The areas colored in yellow show the region as occupied by the magnetic flux belonging to pre-eruption MFR, i.e., the original component of the erupting MFR. Middle: The upward component of Lorentz force F_z as divided by density ρ. Right: The vertical velocity v_z. Time proceeds from top to bottom: the first moment is close to the onset time of the eruption, and the last moment is close to the peak time of the eruption acceleration.

MFR through the continuous reconnection during the eruption, which will be called the “reconnected component”, and the work associated with this component should be attributed to the reconnection, since this work does not exist without reconnection. The reconnected component wraps the original component and both expand in volume during the eruption.

We calculated the magnetic squashing degree (Q factor) to identify the quasi-separatrix layers (QSLs) (Liu et al. 2016) that define the 3D boundary of the entire erupting MFR, for which the volume is denoted as $V_e(t)$. In practice, it does not need to compute the Q factor in the full 3D volume (which is extremely time-consuming) but only on the central cross section of the volume (i.e., the $y = 0$ slice in our case). The QSLs on the slice define a closed area separating the MFR from the ambient field, which are shown in the left column of Figure 6. We traced all magnetic field lines that pass through the grid points within the closed area. Each of these field lines defines an elementary flux tube that constitutes the MFR, and $V_e(t)$ is the sum of the volumes of all these flux tubes. Since the axial flux of the elementary flux tube is conserved along the tube, the cross section of the flux tube at different positions is inverse to its local magnetic field strength, and thereby the volume of the flux tube can be obtained easily. The original component is obtained by tracing the field lines (or the elementary flux tubes) that root in the same footpoints of the MFR at the eruption onset time, and the volume is denoted as $V_o(t)$. Then the volume occupied by the reconnected component, $V_r(t)$ is obtained by subtracting the original component from the entire MFR, $V_r(t) = V_e(t) - V_o(t)$. In the left column of Figure 6, the original component at different times is denoted by the yellow area on the $y = 0$ slice. With these volumes determined, we can calculate the powers and works done by the upward Lorentz force $F_z = (\mathbf{J} \times \mathbf{B})_z$ in these two components of the MFR using the following formulas,

$$P_c(t) = \int_{V_c, F_z>0, v_z>0} F_z v_z \mathrm{d}V,$$

$$W_c(t) = \int_{t_{\mathrm{onset}}}^{t} P_c(t)\mathrm{d}t, \qquad (3)$$

where the subscript c refers to o (by the original component), r (reconnection component), or e (entire). By restricting the computation within domain of $F_z > 0$ and $v_z > 0$, the power and work as obtained account for the upward acceleration of the eruption.

The results are shown in Figure 7 for the simulation run RES0 (other runs have almost the same results and are thus not shown) with time starting from the onset of the eruption. In comparison, the evolution of kinetic energy is also shown in the figure. With start of the eruption, the powers (P_e, P_o, and P_r) first increase to their peak values at around $t = 55$ min and then decrease (Figure 7A). This is consistent with time profile of the kinetic energy increasing rate, which also reaches its peak at nearly $t = 55$ min. At the beginning, P_o (the black solid line) is large than P_r (the green solid line), but is quickly overtaken by the latter after about 1 min. This is clearly seen from the ratio of P_r/P_o, which increases to a high value of 5 near the peak time, showing that the reconnected component dominates the acceleration of the eruption at the peak time. As seen in Figure 7B, all the works continuously increase, consistent with the profile of the kinetic energy. Also same as the profiles of the power, the work done by the reconnected component W_r increases much faster than the original component W_o, and exceeds well W_o after around $t = 52$ min. At $t = 56$ min, W_r is 3.8 times of W_o (see the ratio W_r/W_o), and thus it accounts for over 79% of the total work. The dominant role of the reconnected flux in driving the eruption can be appreciated by inspecting the distribution of the Lorentz force in the erupting MFR, which is shown in the middle column of Figure 6. The upward acceleration by the Lorentz force F_z/ρ is mainly distributed in the lower part of the erupting MFR, i.e., in the newly reconnected flux that joins in the MFR from the reconnection site, while the acceleration at the original component of MFR is much weaker. Therefore the original component is mainly pushed upward from below by the reconnected component. Consequently, the lower part of the original component (the yellow area in the left column of Figure 6) is compressed upward substantially, and its boundary is transformed from an upward concave shape to a downward concave one.

This analysis indicates that the work done by reconnected component plays a major role in driving the eruption, while the original component only contributes a small part to the driving force of the eruption. In other words, reconnection plays a more important role in driving the eruption, while torus instability is only a minor contributor to the driving force of the eruption.

4 CONCLUSIONS

To summarize, we have developed a numerical model of solar eruption of a pre-existing coronal MFR in which both the ideal and resistive processes contribute to the initiation process but the latter plays the primary role. Unlike many other models that start from an unstable MFR configuration and use some kind of disturbance to trigger the eruption, we first constructed a stable MFR enclosed by a background field by relaxing a TDm MFR (utilizing the RBSL method) to an MHD equilibrium. This initial state was then driven to evolve into an eruption by a continuous converging motion of the footpoints of background field at the bottom surface. Therefore our model can show the self-consistent transition from a stable equilibrium to an eruption as driven by photospheric motions. The coronal magnetic field underwent first a quasi-static energy storage phase, in which magnetic energy is gradually injected through the Poynting flux as introduced by the converging flow. In this quasi-static evolution phase, the MFR is driven to rise slowly with the decay index at the apex of rope axis increases continuously. Meanwhile, a thin current layer is formed beneath the MFR, as a result of the rise of the MFR and the converging of the background arcade.

Interestingly, the eruption is initiated at a critical point when two conditions are met almost simultaneously. Firstly, the MFR axis reaches a height where the decay index reaches very close to $n_c = 1.5$, which is consistent with the canonical threshold of the torus instability. Secondly the current layer is thinned to a current sheet and reconnection sets in. The first condition seems to indicate that the torus instability triggers the eruption and the decay index plays a crucial role in determining the occurrence of eruptions, while the second condition appears to infer that the eruption is actually triggered by reconnection. To clarify this issue, we have analyzed the profiles of the hoop force and strapping force at the MFR axis, and found that these forces are well balanced

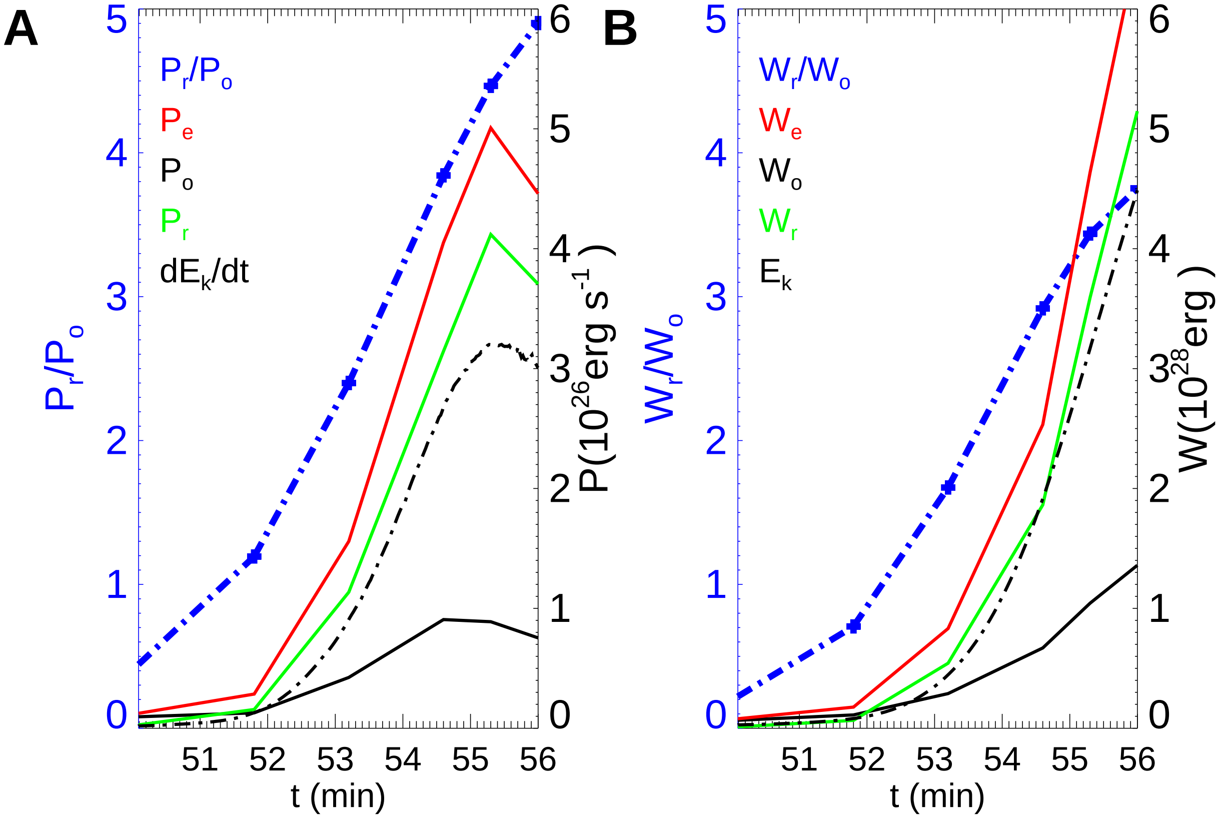

Figure 7. Evolution of the powers (A) and works (B) done by the Lorentz force of the erupting MFR that drives the upward acceleration of the eruption. The time starts from the onset of the eruption $t = 50$ min 09 s. The red solid lines represent the power and work done by the entire MFR, P_e and W_e. The black solid lines represent the those done by original component of the MFR, P_o and W_o. The green solid lines represents those as contributed by the newly reconnected component of the erupting MFR, P_r and W_r. The black dashed line in A are shown for increasing rate of the kinetic energy, and in B for evolution of kinetic energy. The blue dashed lines represent the ratio of powers (A) and works (B) from the reconnected component to those from the original component.

at the eruption onset time, suggesting that the eruption is not triggered by torus instability. Additionally, we have performed experiments with different grid resolutions and found that the eruption is postponed with higher resolutions, which highlights the significance of reconnection in determining the timing of eruption, because at a higher resolution a current sheet is thinner and the onset time of reconnection is postponed. We further analyzed the driving force for the acceleration of the eruption by quantifying separately the work by the original MFR (which exists before the eruption) and that by the newly reconnected magnetic flux that joins in the erupting MFR. It is found that the work done by the reconnected component accounts for a major part (about 80%) in the total work done by the MFR during the eruption. This stresses the importance in of reconnection in driving the eruption. Therefore our study suggests that, even in the situation with a pre-existing coronal MFR, reconnection could play a primary role in triggering and driving its eruption.

The key scenario as demonstrated in this paper, that is, a current sheet is formed during the quasi-static evolution phase and eruption is mainly initiated by the reconnection at the current sheet, is essentially identical to the fundamental mechanism as shown in recent high-resolution simulations (Jiang et al. 2021a; Bian et al. 2022b,c) for a single sheared arcade (without pre-existing MFR). Therefore our study shows that the fundamental mechanism can also be extended to the situation even with a pre-existing MFR. This study also suggests that the pre-existence of MFR, as often found before eruption, does not necessarily indicate the ideal instabilities as being responsible for the eruption. This is consistent with recent observational studies. For example, by a survey of the major flares (above GOES M5.0) from 2011 to 2017 with coronal magnetic field extrapolations, Duan et al. (2019) shows that nearly 90% of the events possess pre-flare MFRs, which indicates that the pre-existence of MFR is rather common for major flares. However, there are over half of MFR-possessing events cannot be explained by the MFR instabilities, since for these events the controlling parameters (decay index and twist degree) of the MFR before flare are apparently below their thresholds for triggering the MFR instabilities. Duan et al. (2019) concluded that these events might be triggered by magnetic reconnection rather than MHD instabilities, and the scenario as shown in this study may apply to these events. Moreover, cautions should be taken when interpreting the eruption initiation by the torus instability using the decay index, since our study suggests that although the decay index is close to the threshold, the eruption only begins with onset of the reconnection.

Nevertheless, it should be noted that our model is much more simplified if compared to the realistic events, which has a higher degree of complexity in either the coronal configuration and the photospheric motions (Jiang 2022). Future studies will be performed using data-constrained and data-driven simulations (Jiang et al. 2022) for real events to disclose the key mechanism in triggering and driving solar eruptions.

ACKNOWLEDGEMENTS

This work is jointly supported by National Natural Science Foundation of China (NSFC 42174200), Shenzhen Science and Technology Program (Grant No. RCJC20210609104422048), Shenzhen Technology Project JCYJ20190806142609035, Shenzhen Key Laboratory Launching Project (No. ZDSYS20210702140800001), Guangdong Basic and Applied Basic Research Foundation (2023B1515040021) and the Fundamental Research Funds for the Central Universities (Grant No. HIT.OCEF.2023047). The computational work was carried out on TianHe-1(A), National Supercomputer Center in Tianjin, China.

DATA AVAILABILITY

All the data generated for this paper are available from the authors upon request.

REFERENCES

Amari T., Luciani J. F., Aly J. J., Mikic Z., Linker J., 2003a, ApJ, 585, 1073

Amari T., Luciani J. F., Aly J. J., Mikic Z., Linker J., 2003b, The Astrophysical Journal, 595, 1231

Antiochos S. K., DeVore C. R., Klimchuk J. A., 1999, The Astrophysical Journal, 510, 485

Aulanier G., Török T., Démoulin P., DeLuca E. E., 2010, ApJ, 708, 314

Bateman G., 1978, MHD instabilities. Cambridge, Mass., MIT Press

Bian X., Jiang C., Feng X., 2022a, Frontiers in Astronomy and Space Sciences, 9, 982108

Bian X., Jiang C., Feng X., Zuo P., Wang Y., Wang X., 2022b, Astronomy & Astrophysics, 658, A174

Bian X., Jiang C., Feng X., Zuo P., Wang Y., 2022c, The Astrophysical Journal Letters, 925, L7

Cheng X., Guo Y., Ding M., 2017, Science China Earth Sciences, 60, 1383

Démoulin P., Aulanier G., 2010, The Astrophysical Journal, 718, 1388

Duan A., Jiang C., He W., Feng X., Zou P., Cui J., 2019, The Astrophysical Journal, 884, 73

Fan Y., 2001, ApJ, 554, L111

Fan Y., 2010, The Astrophysical Journal, 719, 728

Fan Y., Gibson S. E., 2003, The Astrophysical Journal, 589, L105

Fan Y., Gibson S. E., 2007, ApJ, 668, 1232

Guo Y., Xu Y., Ding M. D., Chen P. F., Xia C., Keppens R., 2019, ApJ, 884, L1

Guo J. H., Ni Y. W., Zhou Y. H., Guo Y., Schmieder B., Chen P. F., 2022, A&A, 667, A89

Hood A. W., Priest E. R., 1979, Solar Physics, 64, 303

Jiang C. W., 2022, Reviews of Geophysics and Planetary Physics, 53, 497

Jiang C., Feng X., Zhang J., Zhong D., 2010, Sol. Phys., 267, 463

Jiang C., et al., 2021a, Nature Astronomy, 5, 1126

Jiang C., Bian X., Sun T., Feng X., 2021b, Frontiers in Physics, 9, 224

Jiang C., Feng X., Guo Y., Hu Q., 2022, The Innovation, 3, 100236

Jiang C., Duan A., Zou P., Zhou Z., Bian X., Feng X., Zuo P., Wang Y., 2023, Monthly Notices of the Royal Astronomical Society, 525, 5857

Kliem B., Török T., 2006, Physical Review Letters, 96, 255002

Leake J. E., Linton M. G., Török T., 2013, The Astrophysical Journal, 778, 99

Linker J. A., Mikić Z., Lionello R., Riley P., Amari T., Odstrcil D., 2003, Physics of Plasmas, 10, 1971

Liu R., 2020, Research in Astronomy and Astrophysics, 20, 165

Liu Q., Xia C., 2022, ApJ, 934, L9

Liu R., et al., 2016, ApJ, 818, 148

Liu Z., Jiang C., Feng X., Zuo P., Wang Y., 2023, ApJS, 264, 13

McCauley P. I., Su Y. N., Schanche N., Evans K. E., Su C., McKillop S., Reeves K. K., 2015, Solar Physics, 290, 1703

Mikic Z., Schnack D. D., van Hoven G., 1990, The Astrophysical Journal, 361, 690

Moore R. L., Sterling A. C., Hudson H. S., Lemen J. R., 2001, ApJ, 552, 833

Patsourakos S., et al., 2020, Space Sci. Rev., 216, 131

Sterling A. C., Moore R. L., 2005, The Astrophysical Journal, 630, 1148

Titov V. S., Démoulin P., 1999, A&A, 351, 707

Titov V. S., Török T., Mikic Z., Linker J. A., 2014, ApJ, 790, 163

Titov V. S., Downs C., Mikić Z., Török T., Linker J. A., Caplan R. M., 2018, ApJ, 852, L21

Török T., Kliem B., 2003, Astronomy & Astrophysics, 406, 1043

Török T., Kliem B., 2005, ApJ, 630, L97

Török T., Kliem B., 2007, Astronomische Nachrichten, 328, 743

Török T., Kliem B., Titov V. S., 2004, Astronomy & Astrophysics, 413, L27

Yang Z. H., Tian H., Li W. X., Zhang J. L., Bai X. Y., Gao Y. H., Chen Y. H., 2022, Reviews of Geophysics and Planetary Physics, 53, 379

Zhang J., Dere K. P., Howard R. A., Kundu M. R., White S. M., 2001, The Astrophysical Journal, 559, 452

Zhang Y., Yan X., Wang J., Li Q., Yang L., Xue Z., 2022, ApJ, 933, 200

Zuccarello F. P., Aulanier G., Gilchrist S. A., 2015, The Astrophysical Journal, 814, 126

This paper has been typeset from a TEX/LATEX file prepared by the author.